Frequency Domain Method for Scattering Damping Time Extraction of a Reverberation Chamber Based on Autocorrelation Functions

Tianyuan Jia, Yi Huang, *Senior Member, IEEE*, Qian Xu, Zhihao Tian, Jingyuan Jiang, and Qiang Hua

***Abstract*—The scattering damping time (τ_s) of a reverberation chamber is a very important parameter but hard to obtain accurately. A novel method for extracting this parameter is presented in this article. By utilizing the frequency domain autocorrelation function and the unstirred frequency domain autocorrelation function, τ_s can be directly calculated from measured S-parameters without the need of performing the inverse Fourier transform (IFT). Mathematical derivation is given based on the Wiener–Khinchin theorem, and experimental measurements are conducted for different frequency bands as well as different stirrer configurations to verify the proposed approach. Compared with the conventional IFT-based method, the proposed method does not involve the procedure of manually selecting the fitting range, while still maintains advantages in terms of the independence of the radiation efficiency and input impedance of the measurement antennas.**

***Index Terms*—Autocorrelation function (ACF), reverberation chamber (RC), scattering damping time (τ_s) , stirrer efficiency, total scattering cross section (TSCS), Wiener–Khinchin theorem.**

I. Introduction

THE scattering damping time (τ_s) [1], in the context of a reverberation chamber (RC) [2], gives an indication about how fast its assembled mechanical stirrers can scatter the electromagnetic (EM) waves excited by a transmitting antenna. τ_s is closely related to the equivalent total scattering cross section (TSCS) [1], [3]–[6], which is a widely used parameter to characterize the geometry and movement properties of the stirrer. Moreover, the stirrer efficiency can be defined based on τ_s so as to provide a reliable and repeatable evaluation on the stirrer performance that is independent of the amount of extra loading or the position of the measurement antennas [7]. Stirrers with higher stirrer efficiency can provide better field uniformity [8], [9], more independent samples [10], and improved uncertainty [11] for various RC-based measurement applications [12].

Conventionally, τ_s is extracted based on the slopes of two types of time-domain responses, namely the power delay profile (PDP) [13] and the unstirred power envelope [1], on a logarithmic scale. Therefore, it is necessary to perform the inverse Fourier transform (IFT) to convert S-parameters measured from the vector network analyzer (VNA) into the time domain. Feasible as it is, this commonly used method suffers from several limitations which results in additional sources of errors. First, the ranges of the time domain responses used for the least square fitting are selected empirically [13], and the inaccuracy arises from this procedure becomes more prominent in terms of the τ_s measurement in which the stirrer itself is the object under test (OUT). Second, the noise level of the late-time response is quite high during the τ_s measurement (e.g., only about 15 dB dynamic range for the measurement scenario in [6]), which could reduce the available measurement range. Third, the number of samples required is the same as that of the original frequency response obtained from the VNA, regardless of the desired resolution bandwidth [14].

It is shown in this article that, based on two types of ACFs defined in (1) and (14) in Section II and the Wiener–Khinchin theorem [15], τ_s can be directly extracted from the relevant threshold frequency offset values, and no IFT operation is required. Therefore, the aforementioned limitations and assumptions in the conventional method are eliminated, while its main merits such as the independence of the total efficiency of the measurement antennas have remained.

The rest of this article is organized as follows. Mathematical deduction of the proposed ACF-based method for the measurement of τ_s is given in Section II. Section III elaborates the experimental setup and preparations. Section IV presents comparisons of the measurement results using the IFT-based and ACF-based methods under different scenarios including two frequency bands and three stirrer configurations. Discussions are also given in this section. Finally, Section IV concludes this article.

II. Theory

Let $S_{21}(f, n)$ be the complex transmission coefficient measured at a mechanical stirrer position n and frequency f. By

Manuscript received September 16, 2019; revised January 17, 2020; accepted February 21, 2020. *(Corresponding author: Yi Huang.)*

Tianyuan Jia, Yi Huang, Jingyuan Jiang, and Qiang Hua are with the Department of Electrical Engineering and Electronics, University of Liverpool, L69 3GJ Liverpool, U.K. (e-mail: tianyuan.jia@liverpool.ac.uk; yi.huang@liverpool.ac.uk; psjjian9@liverpool.ac.uk; qiang.hua@liverpool.ac.uk).

Qian Xu is with the College of Electronic and Information Engineering, Nanjing University of Aeronautics and Astronautics, Nanjing 211106, China (e-mail: emxu@foxmail.com).

Zhihao Tian is with the College of Advanced Interdisciplinary Studies, National University of Defense Technology, Changsha 410073, China (e-mail: tian.zhihao@foxmail.com).

Color versions of one or more of the figures in this article are available online at http://ieeexplore.ieee.org.

Digital Object Identifier 10.1109/TEMC.2020.2979014

definition, the frequency domain autocorrelation function (FD-ACF) $R(\partial f, n)$ can be calculated using

$$R\left(\partial f, n\right) = \int_{-\infty}^{+\infty} S_{21}\left(f, n\right) S_{21}^{*}\left(f + \partial f, n\right) df \tag{1}$$

where ∂f stands for the frequency offset for the FD-ACF and $*$ is the complex conjugate operation. For practical measurement scenarios, the frequency band of interest is limited, and the integration interval in (1) is substituted by a finite region.

According to the Wiener–Khinchin theorem [15], the FD-ACF and the time domain PDP essentially constitute a Fourier pair as follows:

$$\begin{aligned} R\left(\partial f, n\right) &= \int_{-\infty}^{+\infty} \mathrm{PDP}\left(t, n\right) e^{-j2\pi\partial f t} dt \\ &= \int_{-\infty}^{+\infty} \left|s_{21}\left(t, n\right)\right|^{2} e^{-j2\pi\partial f t} dt \end{aligned} \tag{2}$$

where $s_{21}(t, n)$ is the time domain transmission coefficient from Antenna 1 to Antenna 2 at one stirrer position, which is the IFT of $\mathrm{S}_{21}(f, n)$

$$s_{21}\left(t, n\right) = \int_{-\infty}^{+\infty} S_{21}\left(f, n\right) e^{j2\pi f t} df \tag{3}$$

and $|s_{21}(t, n)|^2$ is the corresponding PDP. Averaging both sides of (2) with all *N* stirrer positions (covering a full revolution) gives

$$\left\langle R\left(\partial f, n\right)\right\rangle_{N} = \int_{-\infty}^{+\infty} \left\langle \mathrm{PDP}\left(t, n\right)\right\rangle_{N} e^{-j2\pi\partial f t} dt. \tag{4}$$

Provided that the early-time behavior of the RC is neglected, it is proven in [13] that

$$\left\langle \mathrm{PDP}\left(t, n\right)\right\rangle_{N} = \left\langle \left|s_{21}\left(t, n\right)\right|^{2}\right\rangle_{N} = P_0 e^{-\frac{t}{\tau_{RC}}} t > 0 \tag{5}$$

where $\langle\rangle$ denotes the ensemble average over multiple stirrer positions, P_0 is the normalized initial power when $t = 0$ and τ_{RC} means the chamber (decay) time constant. Simplifying the indefinite integral in (4) based on (5), and normalizing the magnitude to its peak value (when $\partial f = 0$) gives [13]

$$\left|\left\langle R\left(\partial f, n\right)\right\rangle_{N}\right|_{\mathrm{norm}} = \frac{1}{\sqrt{1 + \left(2\pi\tau_{\mathrm{RC}}\partial f\right)^{2}}} \tag{6}$$

where $||_{\mathrm{norm}}$ means taking the absolute value and normalizing to the peak value. If a threshold value $\frac{1}{\sqrt{2}}$ is set in (6) [16], we can get

$$\tau_{\mathrm{RC}} = \frac{1}{2\pi\partial f_{\mathrm{th}}} \tag{7}$$

where ∂f_{th} is the reading of the frequency offset when the value of $|\langle R(\partial f, n)\rangle_N|_{\mathrm{norm}}$ drops to $\frac{1}{\sqrt{2}}$. Note that (7) directly relates τ_{RC} to the FD-ACF.

According to the two definitions (from different perspectives) of the quality factor (*Q* factor) for an RC given in [17]

$$Q = \frac{f}{\Delta f} = \omega\tau_{\mathrm{RC}} \tag{8}$$

where Δf is the average mode bandwidth due to different sources of power loss leading to finite *Q*, and ω is the angular frequency. By substituting (8) into (7), we obtain $\partial f_{\mathrm{th}} = \Delta f$, which is the actual physical meaning of ∂f_{th} [18].

Further investigation into $\mathrm{S}_{21}(f, n)$ shows that it consists of two parts [11]

$$S_{21}\left(f, n\right) = S_{21,s}\left(f, n\right) + S_{21,\mathrm{us}}\left(f\right) \tag{9}$$

where $S_{21,s}(f, n)$ is the stirred part that efficiently interacts with the stirrer position *n*, and $S_{21,us}(f)$ is the unstirred part which is defined as [11]

$$S_{21,us}\left(f\right) = \left\langle S_{21}\left(f, n\right)\right\rangle_{N}. \tag{10}$$

The following equation can be derived based on (3) and (10):

$$\left\langle s_{21}\left(t, n\right)\right\rangle_{N} = \int_{-\infty}^{+\infty} S_{21,us}\left(f\right) e^{j2\pi f t} df \tag{11}$$

which indicates that $S_{21,us}(f)$ and $\langle s_{21}(t, n)\rangle_N$ form a Fourier pair. In [1], it is given that

$$\left|\left\langle s_{21}\left(t, n\right)\right\rangle_{N}\right|^{2} = P_o e^{-\frac{t}{\tau_{\mathrm{eq}}}} \quad t > 0 \tag{12}$$

with

$$\frac{1}{\tau_{\mathrm{eq}}} = \frac{1}{\tau_{\mathrm{RC}}} + \frac{1}{\tau_s} \tag{13}$$

where τ_s is the scattering damping time. From (5), (12), and (13), it can be seen that τ_s essentially describes how fast the unstirred power is dissipated relative to that of the total excited power.

Similar to (1), we can define the autocorrelation function based on the unstirred power (or FD-ACFUS for simplicity) which is given as follows:

$$R_{\mathrm{us}}\left(\partial f\right) = \int_{-\infty}^{+\infty} S_{21,\mathrm{us}}\left(f\right) S_{21,\mathrm{us}}^{*}\left(f + \partial f\right) df. \tag{14}$$

Again, based on the Wiener-Khinchin theorem, the following Fourier pair can be derived:

$$R_{\mathrm{us}}\left(\partial f\right) = \int_{-\infty}^{+\infty} \left|\left\langle s_{21}\left(t, n\right)\right\rangle_{N}\right|^{2} e^{-j2\pi\partial f t} dt. \tag{15}$$

Substituting (12) into (15) and normalizing the magnitude to its peak value gives

$$\left|R_{\mathrm{us}}\left(\partial f\right)\right|_{\mathrm{norm}} = \frac{1}{\sqrt{1 + \left(2\pi\tau_{\mathrm{eq}}\partial f\right)^{2}}}. \tag{16}$$

If we also set a threshold value $\frac{1}{\sqrt{2}}$ to (16), then we obtain

$$\partial f_{\mathrm{th2}} = \frac{1}{2\pi\tau_{\mathrm{eq}}} = \frac{1}{2\pi}\left(\frac{1}{\tau_{\mathrm{RC}}} + \frac{1}{\tau_s}\right) \tag{17}$$

where $\partial f_{\mathrm{th2}}$ is the reading of the frequency offset when the value of $|R_{\mathrm{us}}(\partial f)|_{\mathrm{norm}}$ reduces to $\frac{1}{\sqrt{2}}$. Combining (7) and (17) to give

$$\tau_s = \frac{1}{2\pi\left(\partial f_{\mathrm{th2}} - \partial f_{\mathrm{th}}\right)}. \tag{18}$$

Thus, $\tau_s$is extracted directly in the frequency domain from the FD-ACF and FD-ACFUS, and no IFT operation is needed.

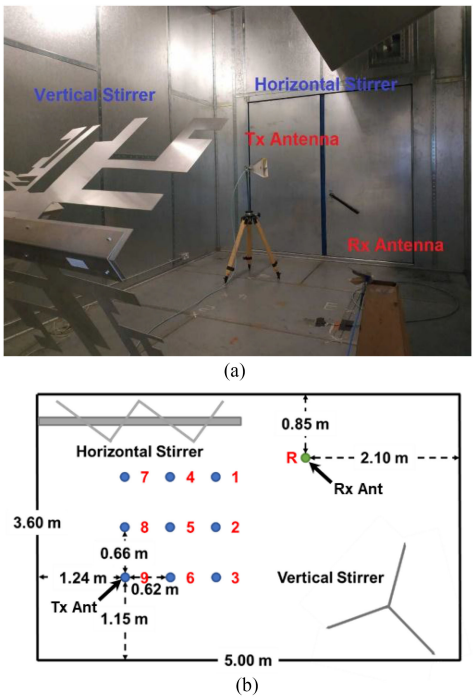

Fig. 1. Typical experimental setup. (a) Measurement scenario. (b) Schematic diagram showing the two stirrers and two antennas.

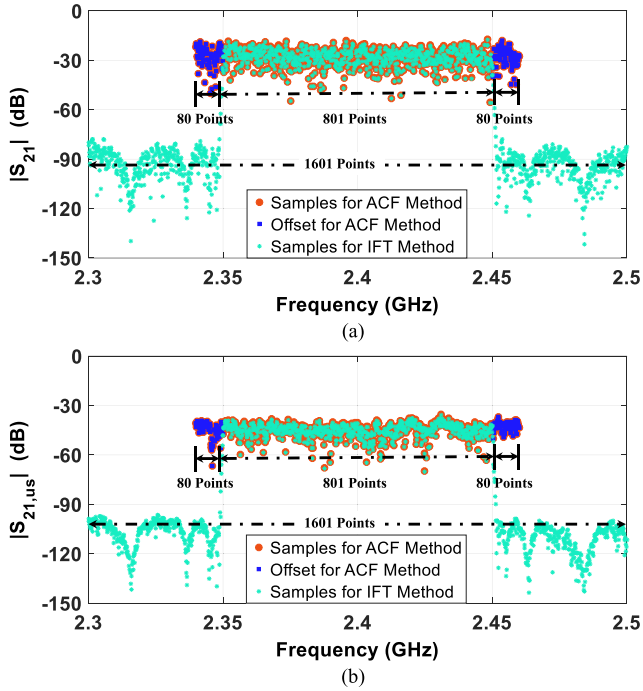

Fig. 2. Frequency samples used for ACF-based and IFT-based methods for 200 MHz bandwidth (2.3–2.5 GHz) and 100 MHz (2.35–2.45 GHz) resolution. (a) S_{21}. (b) $S_{21,us}$.

It is worth emphasizing that there is no explicit term related to radiation efficiency or free space impedance in (18), which indicates that this method does not require prior knowledge for the measurement antennas.

III. Experimental Setup and Preparations

The RC at the University of Liverpool [with dimensions 3.60 (w) $\times$ 5.80 (l) $\times$ 4.00 m (h)] was used for measurements [17]. A typical chamber measurement setup is illustrated in Fig. 1(a). The chamber is furnished with two computer-controlled mechanical stirrers. The receiving antenna (SATIMO SH 2000) was placed at a fixed location [point "R" in Fig. 1(b)] with unchanged orientation (towards the vertical stirrer), polarization (vertical polarization), and height (0.77 m), while the transmitting antenna (Rohde & Schwarz HF 906), with 1.40 m in height, was fixed at point 9 in Fig. 1(b) facing the horizontal stirrer with horizontal polarization. Prior to each measurement, a standard 2-port calibration was performed to move the reference plane from the output ports of the VNA to the input ports of Antenna 1 and Antenna 2. Throughout the whole experimental procedures, the intermediate frequency (IF) bandwidth was chosen to be 10 kHz as a compromise between the noise floor level and the measurement time. The output power was set to -3 dBm. During each measurement, the stirrers were moved in mode-tuning mode with 1° step size to 360 positions to cover a complete revolution. At each stirrer position, a 200-MHz frequency band (giving 5 ns time-domain resolution) was swept with 1601 S_{21} samples, which corresponds to 125-kHz sampling interval, or 8-μs time period, which is long enough to avoid the aliasing effect.

Subsequently, the central 100 MHz was used for τ_{RC} and τ_s extraction. The reason for doing this is to emphasis the function of the frequency domain moving filtering window, which is necessary, especially in wideband measurement scenarios like 5G millimeter Wave (mm-Wave) band characterization, to select narrower sub-bands for improved resolution of the quantity to be measured. For the proposed ACF based approach, samples outside the moving window can be simply discarded. In contrast, for the conventional IFT-based method, a relatively complex BPF (Elliptic, Gaussian, etc.) is generally required and the number of samples needed is the same as that of the original frequency response obtained from the VNA despite the actual frequency resolution.

For illustration, for the case in which the measured frequency response (S_{21} and $S_{21,us}$) is 2.3–2.5 GHz, and parameters (e.g., τ_{RC} and τ_s) are calculated at around 2.4 GHz with 100 MHz frequency resolution (see Fig. 2 for details). It can be seen that the unstirred power is around 15 dB lower than the original power. Fig. 2 also indicates that for the IFT-based method, although only the frequency range 2.35–2.45 GHz is of interest, all the 1601 points are required in order to correctly perform IFT. The proposed method, on the other hand, only needs 961 points (60% that of the IFT based method) by considering a 10 MHz frequency offset band (80 points) on both sides, which saves storage as well as computational resources. It is also flexible to adjust the width of the offset band to adapt to different situations. But this offset band is small compared to the whole bandwidth of the frequency response in practical cases.

Moreover, the above-mentioned scenario will be more prominent for wideband measurement with much more frequency

samples, while a certain frequency resolution is still required for the parameters to be calculated.

In this article, two sets of experiments were conducted to verify the proposed approach. First, measurements were repeated at two different frequency bands, namely the lower band (2.3–2.5 GHz) and the higher band (5.8–6.0 GHz) to check if it is sensitive to frequency bands. Second, three different stirrer configurations (case 1: with both the horizontal stirrer and the vertical stirrer rotating simultaneously; case 2: with the horizontal stirrer only; case 3: with the vertical stirrer only) were examined to evaluate if it is sensitive to stirring. For each measurement, the traditional IFT based method was also performed for comparison purposes, and a 10th order elliptic BPF with 100-MHz passband, 0.5-dB passband ripple, and 60-dB stopband attenuation was used. As aforementioned, τ_s is closely related to the equivalent TSCS and the stirrer efficiency, and these two quantities can be used to verify the proposed method. The equivalent TSCS is, by definition, linked with τ_s by the following equation [1]:

$$\widetilde{\mathrm{TSCS}} = \frac{V}{\tau_s c_0} \tag{19}$$

where V is the volume of the RC and c_0 is the speed of the light in free space. The stirrer efficiency in [7] is defined as

$$\eta_{\mathrm{s}} = 1 - \exp\left(-\frac{12\sqrt[3]{V}}{c_0 \tau_s}\right). \tag{20}$$

To quantify the difference between the parameters obtained using the IFT-based method and the proposed ACF-based method, the following relative discrepancy (described in percentage) is defined

$$D_r\left(x\right) = \frac{|x_{\mathrm{ACF}} - x_{\mathrm{IFT}}|}{x_{\mathrm{ACF}}} \times 100\% \tag{21}$$

where x is the measured quantity, e.g., τ_s, $\widetilde{\mathrm{TSCS}}$, and η_{s}.

IV. Measurements and Discussions

A. Two Different Frequency Bands

In this scenario, the horizontal and vertical stirrers were rotated simultaneously in mode-tuning mode. τ_{RC} extraction in the 2.3–2.5 GHz range is illustrated in Fig. 3. Fig. 3(a) represents the IFT-based approach. The green curve stands for PDP at one arbitrary stirrer position, and the blue curve is the averaged PDP over all 360 stirrer positions. The red dashed line is the least-square fitted result which can be formulated as

$$10\log_{10}\langle \mathrm{PDP}\left(t,n\right)\rangle_N = k_1 t + b \tag{22}$$

with $k_1 = -10/(\tau_{\mathrm{RC}} \ln 10)$ the slope of the fitted line, and $b = 10\log_{10} P_0$ the initial power condition. The time region 250–6000 ns was chosen for linear curve fitting. Result gives $k_1 = -2.98 \times 10^6$, or equivalently, $\tau_{\mathrm{RC,IFT}} = 1459$ ns.

The ACF-based method is depicted in Fig. 3(b). The blue curve stands for the FD-ACF at one arbitrary stirrer position, and the red curve is the averaged FD-ACF over all 360 stirrer positions.∂f_{th} defined in (7) can be read from the abscissa value of the intersection point between the FD-ACF and the black

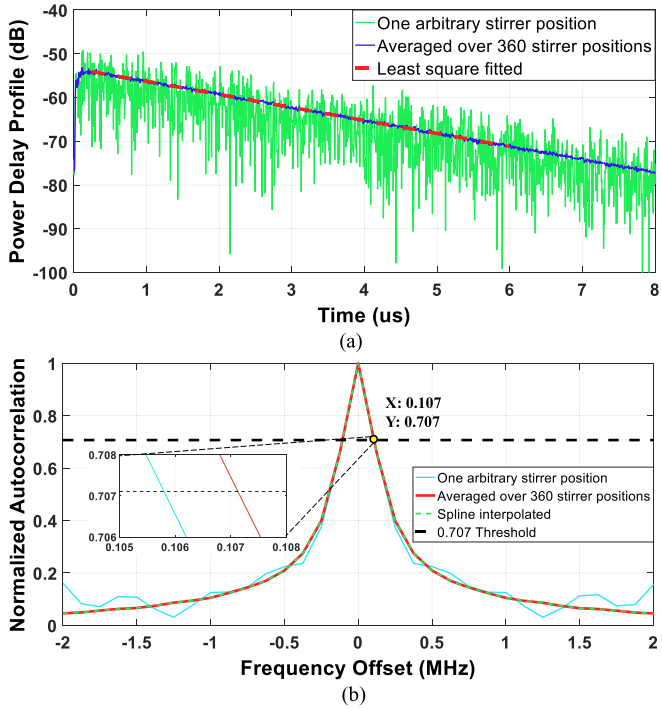

Fig. 3. Extracting τ_{RC} in the frequency range 2.3–2.5 GHz. (a) IFT-based method. (b) ACF-based method.

dashed threshold line. Cubic spline interpolation [19] can be used to increase the density of points [the green dashed line in Fig. 3(b)] of the FD-ACF. As can be seen, $\partial f_{\mathrm{th}} = 107$ kHz, which corresponds to $\tau_{\mathrm{RC,ACF}} = 1487$ ns. Note that using only one arbitrary stirrer position tends to underestimate ∂f_{th}, as can be observed in the zoomed-in subplot in Fig. 3(b). Equivalently, this results in 1.2% overestimation of $\tau_{\mathrm{RC,ACF}}$. Not surprisingly, the further study indicates that this relative discrepancy gradually reduces as the number of stirrer positions used increases. Specifically, when 20 independent stirrer positions are used, the corresponding relative discrepancy is reduced to less than 0.5%.

Similarly, Fig. 4 demonstrates theτ_s extraction procedure for the 2.3–2.5 GHz band. The IFT-based method is illustrated in Fig. 4(a). The blue curve is the unstirred power envelope when the transmitting antenna is fixed at position 9 [as shown in Fig. 1(b)]. The red dashed line is the least-square fitted result, given by

$$10\log_{10}|\langle s_{21}\left(t,n\right)\rangle_N|^2 = k_2 t + b \tag{23}$$

where $k_2 = -10/(\tau_{eq} \ln 10)$ is the slope of the fitted line. Comparing Fig. 4(a) with Fig. 3(a), it can be found that the damping speed of the unstirred power envelope is much faster than that of the PDP. Consequently, a much smaller time interval (50–450 ns) should be selected for the least-square fitting process. The slope k_2 can be extracted accordingly (-5.41×10^7), giving $\tau_{\mathrm{eq,IFT}} = 80$ ns and $\tau_{s,\mathrm{IFT}} = 85$ ns according to (13).

Fig. 4(b) shows the corresponding ACF-based method. $\partial f_{\mathrm{th2}} = 2111$ kHz is directly read from the FD-ACFUS curve, giving $\tau_{s,\mathrm{ACF}} = 79$ ns according to (18). Note that the asymmetric pattern can be observed when the absolute value of ∂f is greater than 4 MHz.

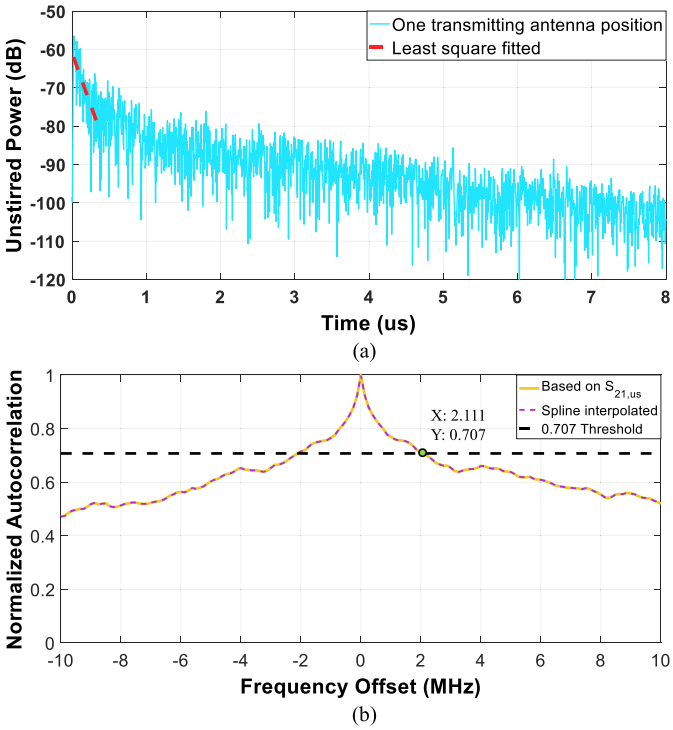

Fig. 4. Extracting τ_s in the frequency range 2.3–2.5 GHz. (a) IFT-based method. (b) ACF-based method.

TABLE I
COMPARISON OF PARAMETERS OBTAINED USING IFT AND ACF METHODS 2.3–2.5 GHZ

Parameter	IFT Based	ACF Based	Relative Discrepancy
τ_s (ns)	85	79	7.6%
$TSCS$ (m^2)	3.28	3.52	6.8%
η_s (%)	87.2	89.1	2.1%

Table I lists a detailed comparison of τ_s, $\widetilde{\text{TSCS}}$ and η_s obtained using both the IFT-based and ACF-based methods. In both cases, more than 3 m^2 $\widetilde{\text{TSCS}}$ (3.28 m^2 and 3.52 m^2, respectively) can be obtained with nearly 90% stirrer efficiency, indicating satisfactory stirrer performance and field uniformity within the RC. Since the stirrer itself is the OUT during τ_s measurement, the fluctuation level of the unstirred power envelope is much larger than that of the averaged PDP, which makes the least-square fitting procedure more difficult and prone-to-error. Combining with other stirring techniques such as source stir could solve this problem, but at the expense of much more data to be measured and much longer measurement time. In contrast, for the ACF-based method, ∂f_{th} and ∂f_{th2} can be obtained easily and straightforward. According to the last column of Table I, relative discrepancies of the three measured quantities are acceptably small (no more than 8%), which verifies that the proposed approach is an effective alternative to the conventional IFT-based method, but with less limitations and assumptions.

To elaborate the effect of manually selecting the time region t on $\tau_{s,\text{IFT}}$ extraction, t is first characterized by two parameters,

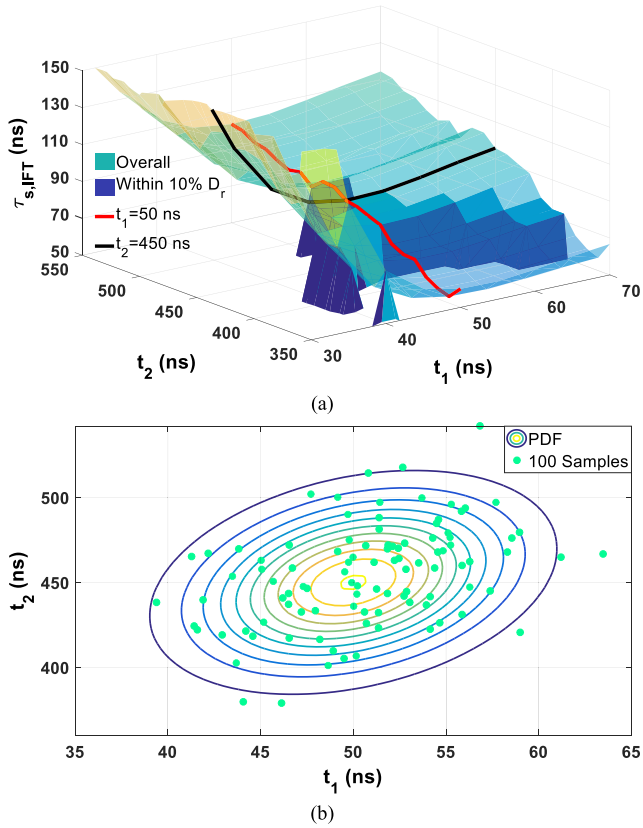

Fig. 5. (a) $\tau_{s,\text{IFT}}$ as a function of t_1 and t_2. (b) Contour representation of the PDF of $t = [t_1, t_2]^T$ and 100 randomly generated samples.

namely the start time (denoted by t_1) and the stop time (denoted by t_2). The extracted $\tau_{s,\text{IFT}}$ can hence be regarded as a function of t_1 and t_2, as illustrated in Fig. 5(a). The 3-D surface, rendered by the parula colormap, covers $\tau_{s,\text{IFT}}$ values for t_1 ranging from 30 to 70 ns and t_2 ranging from 350 to 550 ns. The 3-D histogram highlights the region that the corresponding $\tau_{s,\text{IFT}}$ values are within 10% relative discrepancy compared with $\tau_{s,\text{ACF}}$. The red curve is for $t_1 = 50$ ns, while the black curve is for $t_2 = 450$ ns, and the intersection of the two curves represents the time region adopted in this article for $\tau_{s,\text{IFT}}$ calculation. It can be seen that $\tau_{s,\text{IFT}}$ is more sensitive to t_1 than t_2 within the time region of interest. Especially when t_1 is smaller than 40 ns, $\tau_{s,\text{IFT}}$ will rapidly surge to around 150 ns, nearly twice as the original value. This is because that small t_1 value may include the early time region into slope computation. In contrast, large t_2 value may include the noise floor region into slope computation.

Next, in order to emulate human behavior when selecting the time region, $t = [t_1, t_2]^T$ is modeled as a random vector which follows Gaussian distribution as specified in the following equation:

$$
\begin{aligned}
& t \sim N(\mu, \Sigma) \\
& \mu = [\mu_1, \mu_2]^T = [50, 450]^T \\
& \Sigma = \begin{bmatrix} \sigma_1^2 & \rho\sigma_1\sigma_2 \\ \rho\sigma_1\sigma_2 & \sigma_2^2 \end{bmatrix} = \begin{bmatrix} 25 & 45 \\ 45 & 900 \end{bmatrix}
\end{aligned} \tag{24}
$$

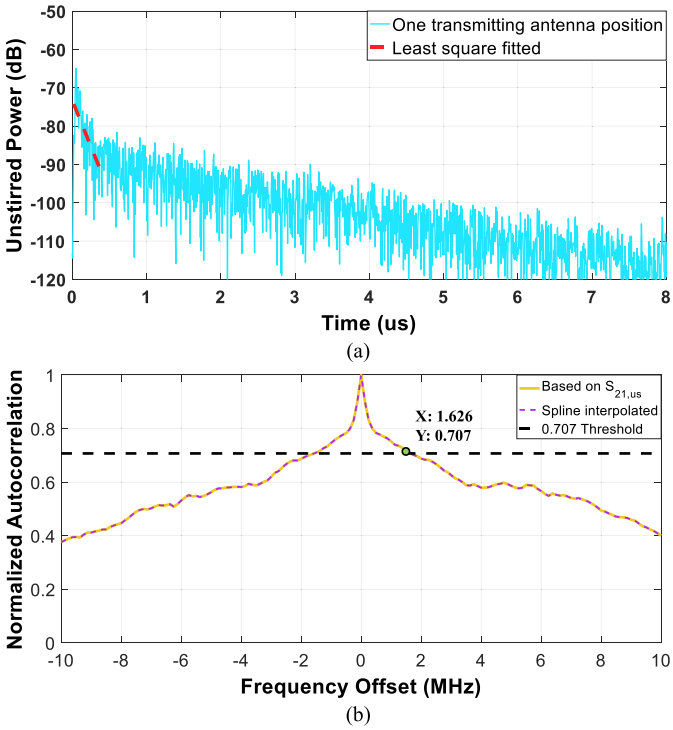

Fig. 6. Extracting τ_s in the frequency range 5.8–6.0 GHz. (a) IFT-based method. (b) ACF-based method.

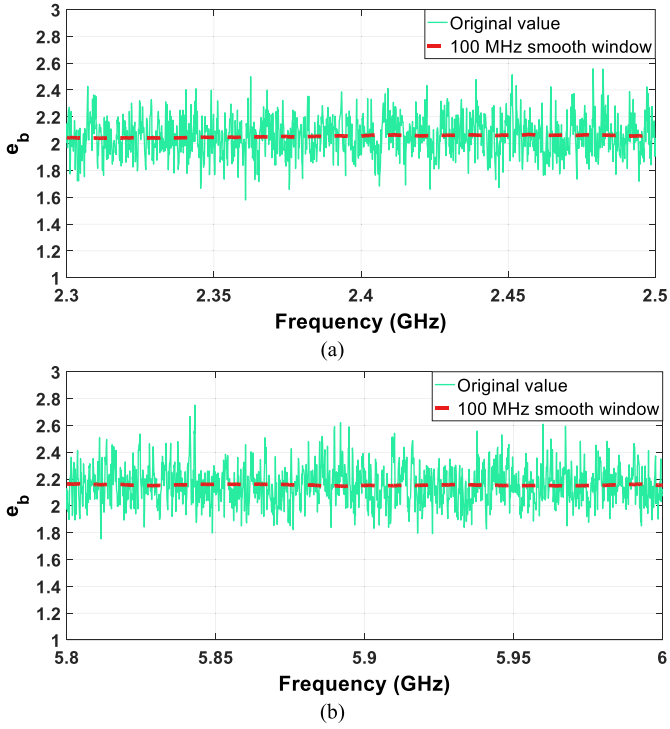

Fig. 7. Measured e_b. (a) 2.3–2.5 GHz. (b) 5.8–6.0 GHz.

TABLE II
COMPARISON OF PARAMETERS OBTAINED USING IFT AND ACF METHODS 5.8–6.0 GHZ

Parameter	IFT Based	ACF Based	Relative Discrepancy
τ_s (ns)	98	107	8.4%
$TSCS$ (m^2)	2.84	2.60	9.2%
η_s (%)	83.2	80.5	3.4%

where μ is the mean vector (with unit ns), Σ is the covariance matrix, σ_1 (5 ns) and σ_2 (30 ns) are the standard deviations of the corresponding variables, and $\rho = 0.3$ is the correlation coefficient. The contour representation of the probability density function (PDF) of t is shown in Fig. 5(b) with 100 randomly generated samples. Result shows that only 34 out of these 100 samples provide $\tau_{s,\mathrm{IFT}}$ values that are within 10% relative discrepancy compared with $\tau_{s,\mathrm{ACF}}$.

For the 5.8–6.0 GHz band, details for obtaining τ_{RC} are omitted due to limited space, with results listed as $\tau_{\mathrm{RC,IFT}} = 1201$ ns and $\tau_{\mathrm{RC,ACF}} = 1179$ ns. Fig. 6 depicts the τ_s extraction processes. The 10-dB drop of the signal level of Fig. 6(a) compared to Fig. 4(a) is due to increased pathloss for higher frequency band. Following the same procedures as the previous measurement, it can be obtained that $k_2 = -4.79 \times 10^7$ and $\partial f_{\mathrm{th2}} = 1626$ kHz, which correspond to$\tau_{s,\mathrm{IFT}} = 98$ ns and $\tau_{s,\mathrm{ACF}} = 107$ ns, respectively.

According to Table II, there is reasonable concordance between the measured results using two methods (relative discrepancy figures are all below 10%). Compared with Table I, values of τ_s calculated at the higher band are larger than that at the lower band, leading to smaller $\widetilde{\mathrm{TSCS}}$ and lower η_s (below 85%). This finding can be validated by utilizing the enhanced backscattering coefficient [20] which is defined as

$$e_b = \frac{\sqrt{\left\langle |S_{11,s}(f,n)|^2 \right\rangle_N \left\langle |S_{22,s}(f,n)|^2 \right\rangle_N}}{\left\langle |S_{21,s}(f,n)|^2 \right\rangle_N} \tag{25}$$

where $S_{*,s}(f,n)$ is the stirred part of the transmission or reflection coefficients,$*$ can be 11, 22, and 21, respectively. Theoretically, e_b equals 2 for an RC working in ideal homogeneous and isotropic condition. Deviation of e_b from its theoretical value manifests the degradation of spatial uniformity. According to Fig. 7, the mean value of e_b (denote as $\bar{e}_b$) at the lower band is 2.05, which implies better spatial uniformity performance than that of the higher band case in which $\bar{e}_b = 2.15$. This is consistent with the τ_s measurement results.

B. Three Different Stirrer Setups

The frequency band was fixed at 2.3–2.5 GHz in this scenario. In addition to the stirrer configuration adopted in Section IV. A (both the horizontal stirrer and the vertical stirrer rotating simultaneously), two more stirrer setups were implemented. First, only the horizontal stirrer was rotated while the vertical stirrer was kept still. It is apparent that the signal shown in Fig. 8(a) decays much slower than that of Fig. 4(a). Hence a longer time interval (50–600 ns) should be chosen for linear fitting. The resultant $\tau_{s,\mathrm{IFT}}$ is 148 ns as derived from the slope value ($k_2 = -3.24 \times 10^7$). The ACF-based method, in contrast, does not require any modification. $\partial f_{\mathrm{th2}} = 1258$ kHz read from

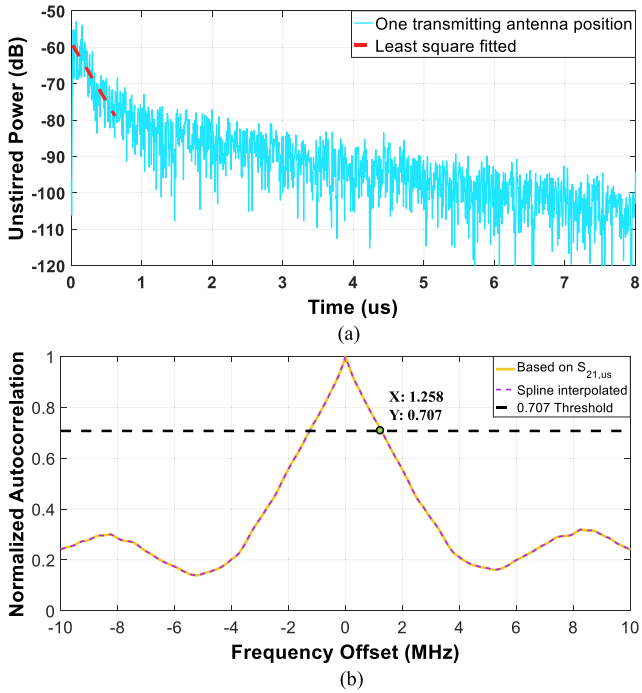

Fig. 8. Extracting τ_s in the frequency range 2.3–2.5 GHz with only the horizontal stirrer. (a) IFT-based method. (b) ACF-based method.

TABLE III
COMPARISON OF PARAMETERS OBTAINED USING IFT AND ACF METHODS WITH HORIZONTAL STIRRER ONLY 2.3–2.5 GHZ

Parameter	IFT Based	ACF Based	Relative Discrepancy
τ_s (ns)	148	139	6.5%
$\widetilde{TSCS}$ (m^2)	1.88	2.00	6.0%
η_s (%)	69.3	71.6	3.2%

TABLE IV
COMPARISON OF PARAMETERS OBTAINED USING IFT AND ACF METHODS WITH VERTICAL STIRRER ONLY 2.3–2.5 GHZ

Parameter	IFT Based	ACF Based	Relative Discrepancy
τ_s (ns)	133	138	3.6%
$\widetilde{TSCS}$ (m^2)	2.09	2.02	3.5%
η_s (%)	73.2	71.9	1.8%

Fig. 8(b) gives $\tau_{s,\mathrm{IFT}} = 139$ ns. Then, we halted the horizontal stirrer and rotated the vertical stirrer instead. Details are omitted here.

Measurement scenarios are summarized in Tables III and IV, respectively. Not surprisingly, the two stirrer setups provide similar $\widetilde{\mathrm{TSCS}}$ (around 2 m^2), due to the fact that the two mechanical stirrers have the similar physical size and they rotate in the same manner about a fixed axis. Overall, the IFT-based method and the proposed ACF method are in good agreement in terms of measured parameters. It is interesting to note that the sum of the $\widetilde{\mathrm{TSCS}}$ of the two single-stirrer scenarios is slightly larger than that of the two-stirrers case. This is because that for the two-stirrers scenario, the horizontal stirrer and the vertical stirrer were rotated simultaneously, which further limits the freedom of movement to some extent.

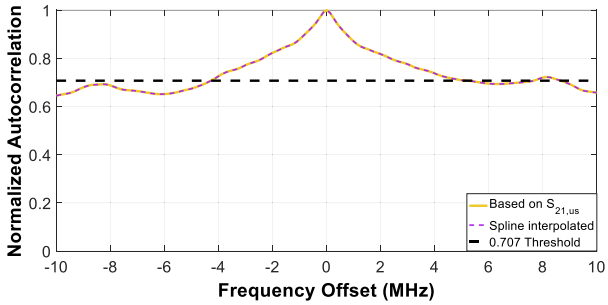

Fig. 9. FD-ACFUS in the frequency range 2.3–2.5 GHz with 3 absorbers loaded into the RC.

V. CONCLUSION

In this article, an alternative way of extracting τ_s based on the FD-ACF and the FD-ACFUS has been presented. In this manner, the IFT operation which is necessary for the currently widely used method can be eliminated. Theoretical derivation of the proposed method has been given, and experimental validations have been performed for both the 2.3–2.5 GHz and 5.8–6.0 GHz bands, as well as for three different stirrer configuration scenarios. Based on the above, conclusion can be drawn that the measured values of τ_s, $\widetilde{\mathrm{TSCS}}$ and η_s using the two methods are generally in good agreement. Furthermore, the data post-processing of the ACF-based method can be greatly simplified, and limitations and assumptions stem from the time region selection process can be effectively avoided.

So far, no analytical expression is available for calculating the ground-truth value of τ_s, except for a relatively loose lower boundary which is derived based on the upper limit of $\widetilde{\mathrm{TSCS}}$ given in [5]st

$$\tau_s^{LB} = \frac{4V}{A_s c_0} \tag{26}$$

where the superscript ^{LB} represents the lower bound, and A_s stands for the stirring surface area. For the two mechanical stirrers installed inside the RC at the University of Liverpool, the total A_s is roughly 8 m^2, which results in $\tau_s^{LB} \approx 14$ ns. In order to obtain a more credible and reliable τ_s value, the IFT-based method and the ACF-based method can be performed simultaneously for cross validation.

Effective as it is, the ACF-based method also has its limitations. First, it requires relatively finer frequency step in order to obtain more accurate ∂f_{th} and $\partial f_{\mathrm{th2}}$ readings, as compared with the IFT-based method in which only the Nyquist theorem is required to be met. In practice, the interpolation technique can be used to relieve this problem. Second, under heavy loading conditions, the normalized $R_{us}(\partial f)$ can be very high that its average value is quite near the threshold value (as illustrated in Fig. 9), which might introduces significant error for τ_s estimation. However, for τ_s extraction, the DUT is the stirrer of the RC, and it should be tested in an empty RC.

Another interesting thing to note is that according to (18), larger $\partial f_{\mathrm{th2}}$ gives smaller τ_s, and thus larger $\widetilde{\mathrm{TSCS}}$ and higher η_{s}. This implies that the FD-ACFUS itself could be an efficient parameter to characterize the stirrer, which also will be a future research direction.

REFERENCES

[1] G. Lerosey and J. D. Rosny, "Scattering cross section measurement in reverberation chamber," *IEEE Trans. Electromagn. Compat.*, vol. 49, no. 2, pp. 280–284, May 2007.

[2] *Electromagnetic Compatibility (EMC)—Part 4–21: Testing and Measurement Techniques – Reverberation Chamber Test Methods*, IEC 61000-421, IEC Standard, Ed 2.0, Jan. 2011.

[3] S. Lallechere, I. E. Baba, P. Bonnet, and F. Paladian, "Total scattering cross section improvements from electromagnetic reverberation chambers modelling and stochastic formalism," in *Proc. 5th European Conf. Antennas Propag.*, Apr. 2011, pp. 81–85.

[4] I. E. Baba, S. Lallechere, P. Bonnet, J. Benoit, and F. Paladian, "Computing total scattering cross section from 3-D reverberation chambers time modeling," in *Proc. Asia-Pacific Symp. Electromagn. Compat.*, May 2012, pp. 585–588.

[5] Q. Xu, Y. Huang, L. Xing, Z. Tian, C. Song, and M. Stanley, "The limit of the total scattering cross section of electrically large stirrers in a reverberation chamber," *IEEE Trans. Electromagn. Compat.*, vol. 58, no. 2, pp. 623–626, Apr. 2016.

[6] Q. Xu, L. Xing, Y. Zhao, T. Loh, T. Jia, and Y. Huang, "The noise level of total scattering cross section measurement in a reverberation chamber," *IEEE Antennas Wireless Propag. Lett.*, vol. 17, no. 10, pp. 1842–1846, Oct. 2018.

[7] Q. Xu, Y. Huang, L. Xing, Z. Tian, M. Stanley, and S. Yuan, "B-scan in a reverberation chamber," *IEEE Trans. Antennas Propag.*, vol. 64, no. 5, pp. 1740–1750, May 2016.

[8] K. A. Remley, C.-M. J. Wang, D. F. Williams, J. J. Aan Den Toorn, and C. L. Holloway, "A significance test for reverberation-chamber measurement uncertainty in total radiated power of wireless devices," *IEEE Trans. Electromagn. Compat.*, vol. 58, no. 1, pp. 207–219, Feb. 2016.

[9] G. Andrieu and N. Ticaud, "Performance comparison and critical examination of the most popular stirring techniques in reverberation chambers using the "Well-Stirred" condition method," *IEEE Trans. Electromagn. Compat.*, vol. 62, no. 1, pp. 3–15, Feb. 2020.

[10] X. Chen, "Experimental investigation of the number of independent samples and the measurement uncertainty in a reverberation chamber," *IEEE Trans. Electromagn. Compat.*, vol. 55, no. 5, pp. 816–824, Oct. 2013.

[11] P.-S. Kildal, X. Chen, C. Orlenius, M. Franzén, and C. S. L. Patané, "Characterization of reverberation chambers for OTA measurements of wireless devices: Physical formulations of channel matrix and new uncertainty formula," *IEEE Trans. Antennas Propag.*, vol. 60, no. 8, pp. 3875–3891, Aug. 2012.

[12] X. Chen *et al.*, "Reverberation chambers for over-the-air tests: An overview of two decades of research," *IEEE Access*, vol. 6, pp. 49129–49143, 2018.

[13] C. L. Holloway, H. A. Shah, R. J. Pirkl, W. F. Young, D. A. Hill, and J. Ladbury, ''Reverberation chamber techniques for determining the radiation and total efficiency of antennas," *IEEE Trans. Antennas Propag.*, vol. 60, no. 4, pp. 1758–1770, Apr. 2012.

[14] X. Zhang, M. P. Robinson, I. D. Flintoft, and J. F. Dawson, "Efficient determination of reverberation chamber time constant," *IEEE Trans. Electromagn. Compat.*, vol. 60, no. 5, pp. 1296–1303, Oct. 2018.

[15] E. W. Weisstein, "Wiener–Khinchin theorem," From MathWorld—A Wolfram Web Resource. [Online]. Available: http://mathworld.wolfram.com/Wiener-KhinchinTheorem.html

[16] Q. Xu, L. Xing, Y. Zhao, Z. Tian, and Y. Huang, "Wiener–khinchin theorem in a reverberation chamber," *IEEE Trans. Electromagn. Compat.*, vol. 61, no. 5, pp. 1399–1407, Oct. 2019.

[17] Q. Xu and Y. Huang, *Anechoic and Reverberation Chambers: Theory, Design and Measurements*. Hoboken, NJ, USA: Wiley, 2019.

[18] X. Chen, P.-S. Kildal, C. Orlenius, and J. Carlsson, "Channel sounding of loaded reverberation chamber for over-the-air testing of wireless devices: Coherence bandwidth versus average mode bandwidth and delay spread," *IEEE Antennas Wireless Propag. Lett.*, vol. 8, pp. 678–681, Jul. 2009.

[19] E. W. Weisstein, "Cubic Spline," From MathWorld–A Wolfram Web Resource. [Online]. Available: http://mathworld.wolfram.com/CubicSpli ne.html

[20] J. M. Ladbury and D. A. Hill, "Enhanced backscatter in a reverberation chamber: Inside every complex problem is a simple solution struggling to get out," in *Proc. IEEE Int. Symp. Electromagn. Compat.*, Jul. 2007, pp. 1–5.

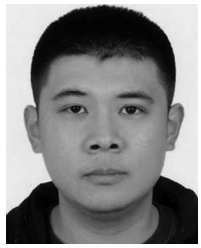

Tianyuan Jia received the B.Eng. degree in telecommunications engineering from Xi'an Jiaotong-Liverpool University, Suzhou, China, in 2012, and the M.Sc. degree in communications and signal processing from Imperial College London, London, U.K., in 2013. He is currently working toward the Ph.D. degree in electrical engineering and electronics at the University of Liverpool, Liverpool, U.K.

His current research interests include reverberation chamber measurement techniques, 5G over-the-air testing, propagation channel modelling and emulation, electromagnetic compatibility testing, statistical electromagnetics, and localization techniques.

Yi Huang (Senior Member, IEEE) received B.Sc. degree in physics from Wuhan University, Wuhan, China, in 1984, the M.Sc. degree in microwave engineering from NRIET, Nanjing, China, in 1987, and D.Phil. degree in communications from the University of Oxford, Oxford, U.K., in 1994.

He has been conducting research in the areas of wireless communications, applied electromagnetics, radar and antennas since 1987. His experience includes three years spent with NRIET as a Radar Engineer and various periods with the Universities of Birmingham, Oxford, U.K., and Essex at the U.K. as a member of research staff. He worked as a Research Fellow at British Telecom Labs, in 1994, and then joined the Department of Electrical Engineering & Electronics, the University of Liverpool, Liverpool, U.K., as a Faculty in 1995, where he is currently a Full Professor in wireless engineering, the Head of High Frequency Engineering Group, and Deputy Head of Department. He has authored or coauthored more than 350 refereed papers in leading international journals and conference proceedings, and authored *Antennas: From Theory to Practice* (John Wiley, 2008) and *Reverberation Chambers: Theory and Applications to EMC and Antenna Measurements* (John Wiley, 2016). He has received many research grants from research councils, government agencies, charity, EU and industry, acted as a consultant to various companies, and served on a number of national and international technical committees and been an Editor, Associate Editor, or Guest Editor of five international journals. He has been a keynote/invited speaker and organiser of many conferences and workshops (e.g., WiCom 2006, 2010, IEEE iWAT2010, LAPC2012, and EuCAP2018). He is currently the Editor-in-Chief of Wireless Engineering and Technology, Associate Editor of IEEE Antennas and Wireless Propagation Letters, UK and Ireland Rep to European Association of Antenna and Propagation (EurAAP), a Fellow of IET, and Senior Fellow of HEA.

Qian Xu received the B.Eng. and M.Eng. degrees from the Department of Electronics and Information, Northwestern Polytechnical University, Xi'an, China, in 2007 and 2010, and the Ph.D. degree in electrical engineering from the University of Liverpool, Liverpool, U.K., in 2016.

He is currently an Associate Professor with the College of Electronic and Information Engineering, Nanjing University of Aeronautics and Astronautics, Nanjing, China. He was as a RF Engineer in Nanjing, China, in 2011, an Application Engineer with CST Company, Shanghai, China, in 2012. His work at the University of Liverpool was sponsored by Rainford EMC Systems Ltd. (now part of Microwave Vision Group) and Centre for Global Eco-Innovation. He has authored the book *Anechoic and Reverberation Chambers: Theory, Design, and Measurements* (Wiley-IEEE, 2019). His research interests include statistical electromagnetics, reverberation chamber, computational electromagnetics, and anechoic chamber.

Zhihao Tian received the B.Sc. degree in optic information science and technology from the National University of Defence Technology (NUDT), Changsha, China, in 2011, and the M.Eng. degree in high power microwave technology, in 2013, in NUDT. He received the Ph.D. degree in electrical engineering with the University of Liverpool, Liverpool, U.K.

He is currently a Research Assistant in NUDT. His research interests include electromagnetic compatibility, statistical electromagnetics, and reverberation chambers.

Jingyuan Jiang received the B.Eng. dual-degree in measuring and controlling technology and instrument from Jilin University, Changchun, China, in 2017, and Tomsk Polytechnic University, Tomsk, Russia, in 2017, and the M.Phil. degree in electrical engineering and electronics from University of Liverpool, Liverpool, U.K., in 2019.

His current research interests include nondestructive testing, deep learning, and artificial intelligence techniques.

Qiang Hua received the B.Sc. degree in communication engineering from The University of Liverpool, Liverpool, U.K., in 2016, and the M.Sc. degree in digital signal processing from The University of Manchester, Manchester, U.K., in 2017. He is currently working toward the Ph.D. degree in base station antennas with The University of Liverpool, Liverpool, U.K.

His current research focuses on the base station antenna design for 5G in wireless communications.